ULTRA-LOW CYCLIC FATIGUE FRACTURE SIMULATION OF BUCKLING-RESTRAINED BRACES AND FRAMES

M. Terashima[1] and G.G. Deierlein[2]

[1] *Ph.D., Nippon Steel Engineering Co., Ltd., Tokyo, Japan, terasihima.masao.mx4@eng.nipponsteel.com*
[2] *Professor, John A. Blume Center for Earthquake Engineering, Stanford University, CA, USA, ggd@stanford.edu*

Abstract

In the past few decades, Buckling-Restrained Braces (BRBs) have been widely implemented in steel-framed structures throughout the world. Since BRBs do not buckle under compressive loading, they display stable and nearly symmetric behavior in tensile and compressive excursions. Thanks to their superior ductility capacity, BRBs have been applied to variety of structures and configurations, such as steel braced frames (i.e. BRBFs), capacity designed outriggers for high-rise buildings, and energy dissipating fuses for rocking-frames. Since the safety of the structures with BRBs heavily relies on the ductility capacity of BRBs, it is important to ensure that BRBs have sufficient fracture resistance to sustain the earthquake-induced inelastic cyclic strain demands.

Provided that BRBs are designed to avoid other premature failure modes (e.g. buckling of casing tube, out-of-plane instability and connection failure), their ductility capacity is typically controlled by fracture of the steel core. Under earthquakes, BRBs will experience a relatively small number of large deformation amplitude cycles, which may lead to failure by Ultra-Low Cyclic Fatigue (ULCF). To date, most of the development and validation of BRB ductility capacity has relied extensively on empirical data from full-scale cyclic loading tests. This nearly exclusive reliance on empirical test data is due in part to the limitation of computational methods for evaluating fracture under inelastic cyclic loading. The lack of reliable analysis methods to evaluate fracture in BRBs limits the capability of BRB designers to develop improved BRB core configurations.

Motivated by the needs mentioned above, this study describes the use of detailed finite element analyses and an ULCF fracture criterion, referred to as the Stress-Weighted Damage Model, to evaluate the inelastic response of BRBs up to the onset of ductile fracture. Practical methods to model the brace buckling restraint conditions are described, along with tests to calibrate the ULCF fracture model. Ductile fracture initiation is evaluated in the yielding and transition zones of the BRB core, considering the effects of fabrication cutting methods, geometric and material imperfections, and loading history. Ductility requirements from BRB qualification tests and standards are compared to ductility demands, considering site-specific earthquake ground motion intensity and duration.

Keywords: Buckling-restrained brace; Ultra-low cyclic fatigue; Finite element analysis

1. Introduction

Since they were invented in Japan about thirty years ago, buckling-restrained braces (BRBs) have applied in high seismic regions throughout the world, primarily as either energy dissipation devices in moment frames or the yielding force resisting component of buckling restrained braced frames (BRBFs). Under strong ground motions, BRBs are subjected to severe cyclic loadings that cause significant inelastic tension-compression deformations of the steel core. With buckling and other modes of failure suppressed, the ductility of BRBs is ultimately controlled by Ultra-Low Cycle Fatigue (ULCF) fracture due to cyclic loading under a small number of cycles (typically less than 100 cycles) with large inelastic strain amplitudes [1]. To date, most of the development and validation of BRB ductility capacity has relied extensively on full-scale cyclic loading tests [2][3]. While UCLF is a typical fracture mode for BRBs, no theoretical or numerical approaches to evaluate BRB fracture caused by ULCF are currently available. Therefore, this study develops an evaluation method to assess BRB fracture based on the underlying micromechanics and detailed Finite Element (FE) simulations. This paper proposes the FE simulation techniques to efficiently replicate unique features of BRBs and investigates what features are likely to influence BRB fracture. Accuracy of the proposed fracture evaluation method is confirmed by comparing the simulation results with observations from full-scale BRB tests, and implications of the BRB ductility on the seismic performance of BRBF systems is discussed.

2. ULCF Fracture Model for BRB Steel Core

2.1 Yielding and Fracture Behavior of BRBs

During large-scale loading tests, BRBs tend to fracture in a few specific locations as shown in Fig.1. One of these locations is the yielding zone. When BRBs fail in this zone, plastic strain localizes in a small region, leading to necking down and ductile fracture at the critical cross-section (Fig.1 (a)). Another common failure location is the transitional zone near the ends of the BRB steel core, where fracture tends to develop more gradually (Fig.1 (b)). In this fracture process, the crack typically initiates and propagates through a ductile tearing mechanism until eventually transitioning into a brittle cleavage fracture. Since cleavage fracture tends to be more statistically random and is highly dependent on the stress fields ahead of the crack tip, it may occur slightly after the ductile crack initiation or longer after ductile crack propagation. Note that this study specifically focuses on evaluating the ductile fracture initiation caused by ULCF. Evaluation of ductile fracture propagation and transition to brittle cleavage fracture is a topic of ongoing research.

(a) Failure in the yielding zone   (b) Failure in the transitional zone

Fig. 1– Typical fracture locations of BRB steel core

2.2 ULCF Fracture Criterion

The micromechanical mechanism of ductile fracture for mild steel used in BRBs is shown in Fig.2. Similar to ductile fracture under monotonic tensile loading, it is well-known that ULCF is caused by nucleation and coalescence of microvoids [4]. Once a ductile crack initiates, local strains and stresses at the crack tip become sufficient to nucleate further microvoids. These voids grow as the crack blunts, and they eventually link with the main crack (i.e. crack propagation). After the ductile crack propagates to a certain length, it often transitions to a brittle fracture mode, referred to as cleavage fracture, resulting in brittle crack propagation and complete failure.
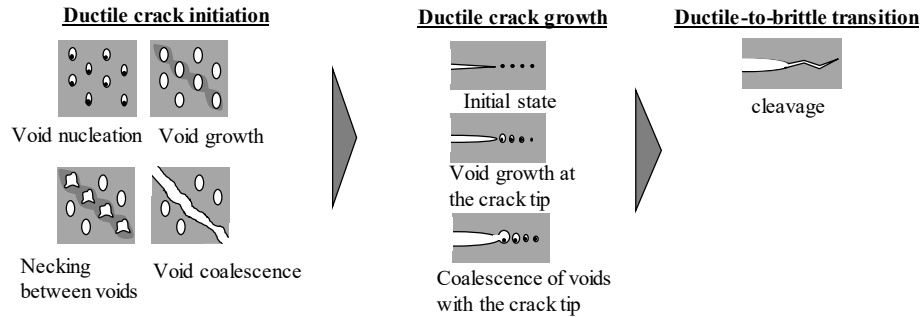
Fig. 2– Micromechanical ductile fracture mechanism of Steel

It has been well-accepted that ductile fracture is caused by microvoid nucleation and coalescence. In the 1960's, Rice and Tracy theorized that under monotonic tensile loading, the critical equivalent plastic strain ($\overline{\varepsilon_p}$) is correlated exponentially with the degree of hydrostatic confinement, referred to as stress triaxiality (*T*). Kanvinde et al. [5] modified this ductile fracture criterion to be applicable to cyclic loading (i.e. ULCF) by considering void shrinkage and material deterioration in compressive cycles. Smith et al. [6] further improved the ductile fracture criterion to be applicable to wide range of stress states and loading conditions. The latest evolution in the local ULCF criterion, the Stress Weighted Damage Model (SWDM), is expressed as follows:

$$D_{SWDM} = e^{\lambda\overline{\varepsilon_{com.}^p}} \cdot \int_{\overline{\varepsilon_p}} C\left(\beta e^{A^+T} - e^{A^-T}\right) \cdot e^{\kappa|\xi|}\, d\overline{\varepsilon_p} \tag{1}$$

where D_{SWDM} is the damage index for ULCF. The material dependent parameters in the equation are calibrated such that fracture is predicted when D_{SWDM} reaches 1.0. The parameters *A+* and *A-* control the triaxiality influence on the growth and shrinkage of voids under positive and negative triaxiality, respectively. β represents the relative rate of void growth and shrinkage under reverse cyclic loading. κ represents the influence of the Lode angle parameter, ξ, which is the smallest angle between the line of pure shear and the projection of the stress tensor on the deviatoric plane. λ controls the rate of capacity degradation due to compressive equivalent plastic strain, $\overline{\varepsilon_{com.}^p}$, and *C* represents overall ductility of the material.

2.3 Calibration of ULCF Cyclic Fatigue Criterion to be used in this study

The FE simulations of the BRBs were performed using nonlinear continuum elements in ABAQUS/standard [7]. This study utilized the von Mises yield surface and Armstrong-Frederick (A-F) model for metal plasticity with combined kinematic and isotropic hardening, including two inelastic backstresses and one isotropic hardening using the following equations:

$$\sigma_Y = \sigma|_0 + \sigma_{iso} + \sigma_{kin.1} + \sigma_{kin.2} \tag{2}$$

$$\sigma_{iso} = Q_\infty\left(1 - e^{-b\overline{\varepsilon_p}}\right) \tag{3}$$

$$\sigma_{kin,1} = \frac{C_1}{\gamma_1}(1 - e^{-\gamma_1\varepsilon_p}) \tag{4}$$

$$\sigma_{kin,2} = \frac{C_2}{\gamma_2}(1 - e^{-\gamma_2\varepsilon_p}) \tag{5}$$

where $\sigma|_0$, σ_{iso}, $\sigma_{kin,1}$, and $\sigma_{kin,2}$ are the initial yield stress, the isotropic hardening component and the kinematic hardening components, respectively. The instantaneous yield stress (σ_Y) is equal to the sum of these stress terms. Eq. (3) represents the isotropic hardening components based on parameters, Q_∞ and *b*, while Eq. (4) and Eq. (5) represent the kinematic hardening based on parameters, C_1, C_2, γ_1 and γ_2, respectively.

3

The plasticity parameters were calibrated using data from standard ASTM-E8 tension bar tests and cylindrical notched bar tests (Fig.3) of A36 steel used to fabricate BRB test specimens. In addition to standard load-deflection data, the deformed geometry of the test coupons was recorded using a digital imaging correlation (DIC) system. The monotonic and cyclic material parameters were determined by minimizing error between coupon test data and the FE models using an optimization routine employing Particle Swarm Optimization [6], yielding the following parameter values:

$$\sigma|_0 : 187.5(MPa), Q_\infty : 199.9(MPa), b : 2.6, C_1 : 77863.0(MPa), C_2 : 1352.0(MPa), \gamma_1 : 574, \gamma_2 : 9.5$$

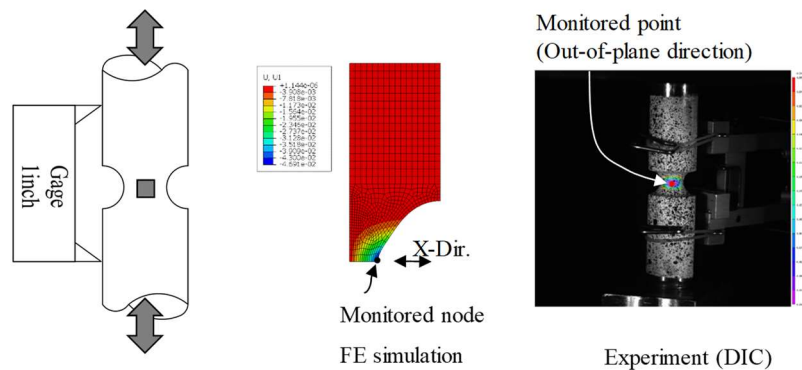Details of the tests, calibration process are summarized by Terashima [8].

Fig. 3– Calibration specimens for cyclic plasticity and SWDM fracture models
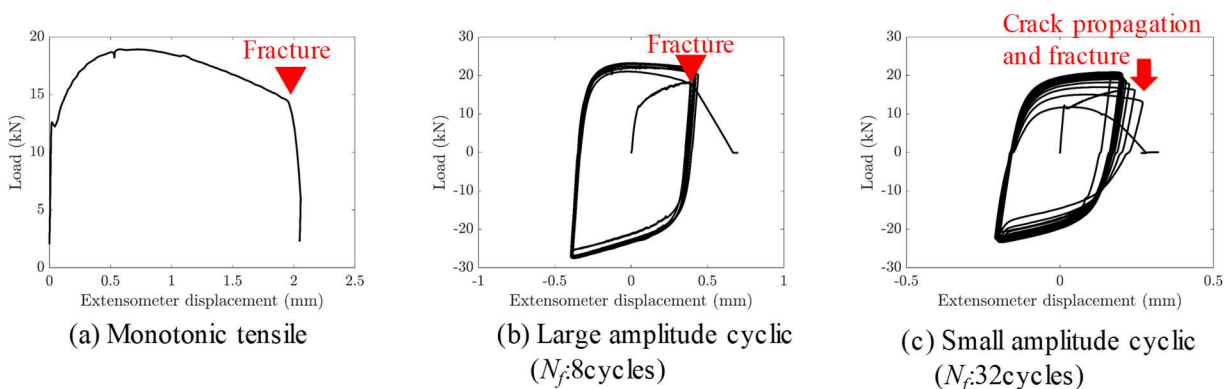

Fig. 4– Illustrative response of CN calibration specimens

Shown in Fig.4 are representative data from cylindrical notched bar tests under monotonic and cyclic loading. By concentrating yielding in the notched portion and varying the notch radius, the cylindrical notched bar provides an effective specimen to interrogate the steel material under varying amounts of triaxiality and cyclic loading regimes. The three results in Fig.4 represent cases that fractured under monotonic tension loading and reverse (symmetric) cyclic loading to displacements equal to about 20% and 10% of the displacement for monotonic failure. For smaller strain amplitudes, where the specimen undergoes many cycles before failure (e.g. 32 cycles in test loaded to 10% of the montonic fracture deformation), the response indicates the presences of graduate ductile crack opening and closing prior to final failure. This is evident from the gradual strength degradation and the slight pinching response in the negative (compression) loading region. For larger strain amplitudes (e.g. 8 cycles in the test loaded to 20% of the monotonic fracture deformation), the slight degradation suggests that there is relatively little ductile crack growth before failure.

In addition to the cylindrical notched bar tests, calibration of the SWDM included tests of grooved plate and square notched bars to vary the loading angle parameter (see [8]). These calibration tests on the ASTM A36 steel resulted in the following parameters for the SWDM (Eq. (1)) [8]:

4

$A+=A-$:1.3, β:1.30, κ:0.33, λ:0.22, $\mu_{lnC} = -1.8166$ ($\mu_C = 0$:1543), $\sigma_{lnC} = 0.3242$, ($COV = 0.17$)

where the most important parameter defining the ductile fracture strain capacity is the median value of the C coefficient, $\mu_{lnC} = -1.82$ (or $\mu_C = 0.15$), which has a coefficient of variation of 0.17 (17%).

3. Finite Element Simulation of BRB Yielding and Fracture

3.1 Buckling-restraining mechanism

Beyond modeling of the steel core material, an important consideration is modeling of the buckling-restraining mechanism in the BRB. Fig.5 schematically illustrates the buckling-restraining mechanism, showing the cross-sectional view along the steel core. The steel core resists the axial force, while the mortar and casing tube, referred to as restraining members, prevent the steel core from global buckling. A thin layer of debonding (or gap) material between the steel core and mortar helps ensure that axial force is not transferred between the steel core and the mortar. This mechanism enables the steel core to deform independently from the restraining members in the axial direction. Since the debonding layer is flexible compared to the steel and mortar, the steel core can undergo slight buckling movement in the out-of-plane direction until it contacts the mortar under compressive loading. The out-of-plane deformation is constrained by contact with the mortar, leading to the high-mode buckling shape shown in Fig.5. As shown in the photograph in Fig.5, this buckling behavior is evident in marks on the cores of BRBs that have been dissected after testing.
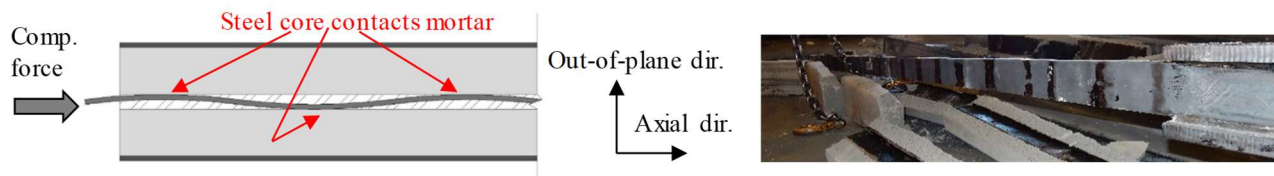

Fig. 5– Schematics of buckling-restraining mechanism

Several studies have simulated the buckling-restraining mechanism by physically modeling the restraining members and applying contact surfaces between the mortar and steel core (e.g. [9][10]). While this approach can replicate high-mode buckling and interaction between the steel core and mortar, it is computationally expensive. Since the primary purpose of this study is to develop an efficient fracture evaluation method, as described in the next section, a simpler approach to represent the buckling-restraining mechanism was employed.

3.2 Finite element modeling of BRBs

Fig.6 shows an example of the FE model developed in ABAQUS [7], where the core and other steel components are modeled using four-node brick elements with reduced integration (C3D8R in ABAQUS). Typically, the core is modeled with four brick elements through the thickness. In the out-of-plane direction, nonlinear spring constraints are attached to the nodes on the steel core (Fig.6 (a)) to resist buckling. These nonlinear springs have nearly zero stiffness for the first 1mm of displacement, representing the thickness of the debonding layer, after which the stiffness rapidly increases, representing the constraint effect when the steel core contacts the mortar encasement. This approach allows the steel core to form high-mode buckling, thereby replicating the behavior of the steel core efficiently. Note that this model assumes that any longitudinal friction transfer between the steel core and mortar is negligible.

As shown in Fig.6 (b), in-plane constraint is provided by modeling the casing tube using beam elements, with linear constraints assigned between nodes on the steel core and the corresponding nodes on the casing tube. Note that the contribution of the mortar to the flexural stiffness of the casing is assumed to be negligible, and the properties of the beam elements are calculated based on those of the steel casing.
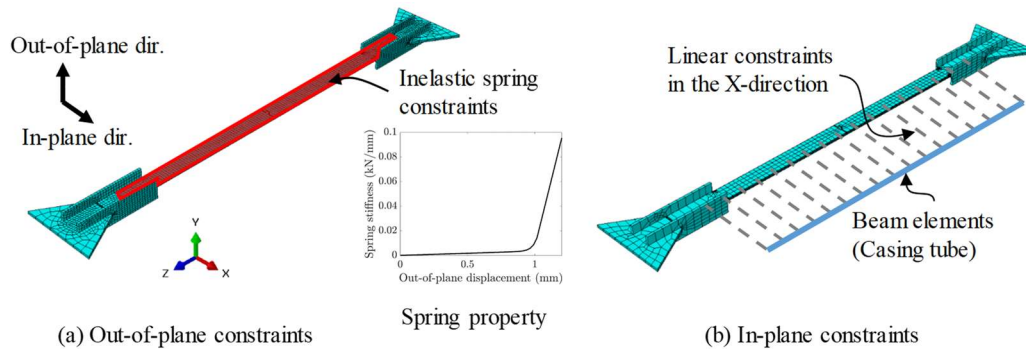
5

(a) Out-of-plane constraints

Spring property

(b) In-plane constraints

Fig. 6– Continuum FE model of BRB core, transition and end conditions

3.3 FE model validation

Shown in Fig.7 is a comparison between the FE simulation results and experimental data for full-scale BRB. The BRB is fabricated with ASTM A36 (measured yield stress of 300 MPa), a core cross section area of 3,750 mm² (25mm x 150 mm) and a core yield zone length of 3007 mm. As shown in Fig.7, the FE simulation successfully captured the global hysteresis of the BRB test.

In addition to capturing the overall load-deformation response, the FE model was also able to capture the compression adjustment factor β ($=C_{max}/T_{max}$) [11]. The differences of maximum forces in tension and compression occur due to the combination of the change of the cross-section area in tension and compression caused by the Poisson effect and interaction between the mortar and steel core. The adjustment factor for the BRB response data shown in Fig.7 was $\beta = 1.09$ from the FE simulation, which was quite close to the value of $\beta = 1.10$ measured in the experiment. Both of these values are close to the theoretical compressive overstrength due to the Poisson effect, β_p, which can be computed using the following equation [12]:

$$\beta_p \approx 1 + \varepsilon \tag{6}$$

where ε is the maximum brace strain demand. Using the strain demand of $\varepsilon = 2*0.035$, the calculated β_p is equal to 1.07. Similar values were calculated and measured for other tests simulated by Terashima [8]. These results indicate that for the BRB specimens considered, there is relatively little interaction between the steel core and mortar, which substantiates assumed boundary conditions used in the analysis (Fig.6). It is important to note that the β values may significantly differ depending on BRB configurations and brace manufacturers [12]. Therefore, for BRBs with β values that are significantly larger than β_p, the interaction between the mortar and steel core may be required in the FE simulations.
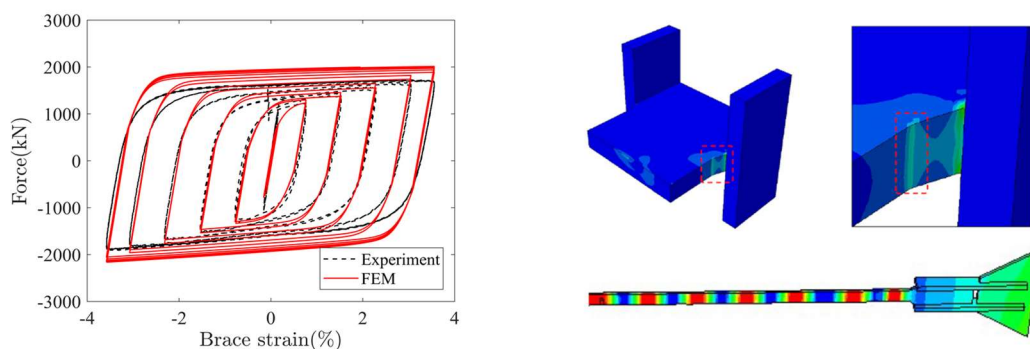

Fig. 7– Comparison of load-displacement curves obtained from FE simulation with the one obtained fom the experimental result (BRB specimen WPSC3A)

6

3.4 Influences of BRB unique features on ductile fracture

Since fracture evaluation is very sensitive to the local stress/strain conditions and fracture toughness at which a crack initiates, we need to carefully investigate the influence of BRB unique features on the ductile fracture evaluation. In this study, the following three factors were investigated to assess their possible influence of the ductile fracture initiation; 1) cutting edge surface condition, 2) geometric and material property variations in the steel core and 3) loading conditions.

3.4.1 Cutting edge surface condition

For most commercial BRBs, the steel cores are cut by a plasma cutting machine. The plasma arc introduces heat during cutting process, thereby changing the micromechanical characteristics along the cutting surface. Since the heat-affected zones (HAZs) tend to be harder and less ductile than the original material (hereinafter referred to as base metal), they may impact the ductility of BRBs when fracture initiates from the cutting surfaces. This study assumed that the effects of plasma cutting can be represented by increasing the yield stress in the A-F parameters and reducing the ductile fracture toughness (i.e. *C* in Eq.(1)) in the HAZs. This assumption is not ideal, but is made for practical reasons, since it is impossible to create coupon-scale specimens purely made of the HAZs.

To evaluate the ductile fracture capacity in the HAZ, small-scale loading tests were conducted using small-scale plate specimens with a 2 mm radius notch, referred to as Blunt-Notch (BN) specimens (Fig.8). The notches of the BN specimens were fabricated by either machine cutting or plasma cutting so as to contrast the differences and to help quantify the influence of the HAZ in the plasma cut cases. The effect on plasma cutting on the yield strength was evaluated by inferring the yield strength from Vickers hardness measurements made through the HAZ thickness. This study employed a model by Pavlina and Van Tyne to relate hardness to yield strength [13]. Based on Vickers hardness measurements, the thickness of the HAZs was assumed to extend into the steel 1mm from cutting surface, and the yield stress values were approximated as three discrete values for FEM modeling using the average values over the each given distance range, as 965MPa, 530Mpa and 380MPa, respectively, for the highlighted zones in Fig.8.

The BN specimens were subjected to reverse cyclic loading, results from which were compared to FE simulations. Observations of fracture initiation in the BN specimens was then used to back calculate the SWDM fracture parameters for the HAZ material. Using Maximum Likelihood Estimation (MLE) algorithm to calibrate the *C* value in the SWDM, and with all other parameters fixed to the values for base metal, the following values were obtained:

$$\mu_{lnC} = 0.2247 \ (\mu_C = 0.78), \sigma_{lnC} = 0.2096$$

Comparing these to the values for the base metal reported previously, the mean value of *C* for the HAZ is approximately 5.5 times larger than that of the base metal ($\mu_C = 0.14$), indicating that the ductile fracture capacity in the plasma-cut HAZ is about 18% (1/5.5) that of the base metal. The variation in cutting surface yield strength and fracture toughness was carried through the FE analyses of the BRBs, all of which were fabricated by plasma cutting without any special post-cutting treatment (e.g. without subsequent grinding of the cutting surface).
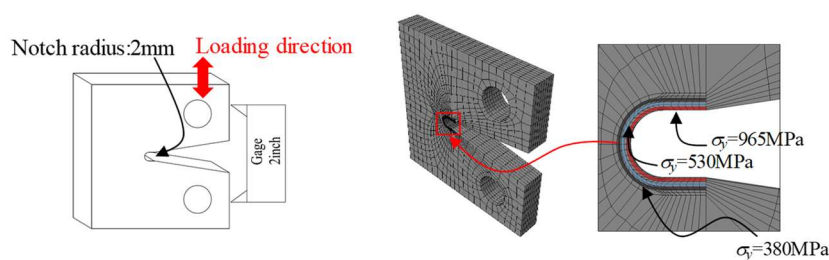

Fig. 8 – Schematics of the BN specimen and FE model

7

3.4.2 Geometric and material variability in the steel core

While the material properties of the steel core are uniform, the steel will inevitably have slight variability through the cross-section and along the length. Moreover, there are slight variations in the cross-section geometry due to imperfections in the plate thickness and the plasma cutting. These slight variations lead to stress/strain localization in the yielding zone (i.e. necking) and, depending on their magnitude, can significantly influence the onset of localization. To explicitly include the influence of the mechanical weakness on necking in FE models, a small cross-section reduction was applied to the yielding zone of the steel core. This cross-sectional reduction was assumed to represent the combined effect of the heterogeneity of material properties and geometric imperfection. A numerical parametric study was conducted with varying the amount of the cross-section reduction to investigate how the mechanical weakness influences necking occurrence.

Comparative analyses of BRB specimens subjected to small plastic strain amplitudes (~3.5%, such as shown in Fig.7) with larger plastic strain amplitudes (~7%) indicate that the initiation of necking and fracture is much more sensitive to imperfections in the small strain amplitude cases. Based on the comparative analyses of this numerical study that included reasonable variations in material parameters (yield strength and hardening modulus) and core geometry, we determined that a 1% reduction in cross-section area seems to be a reasonable representation of variability that leads to onset of necking that is consistent with the test observations. While the variability is applied to the geometry of the FE model, the 1% variation is considered as representative of both material and geometric imperfections.

3.4.3 Loading type

The AISC seismic design provisions [14] specify two loading protocols for qualification testing of BRBs. The so-called uniaxial loading involves applying displacements parallel to the BRB axis, and the second, subassemblage loading, involves simultaneous application of displacements both parallel and transverse to the member. Not surprisingly, past experiments indicate that specimens subjected to subassemblage loading are more likely to fail in the transitional zone, due to additional strain concentration caused by rotational loading, resulting in earlier fracture than specimens subjected to uniaxial loading [15][16]. Shown in Fig.9 are illustrative results of FE analyses of a BRB that was subjected to uniaxial and subassemblage loading, where the uniaxial cumulative plastic displacement (CPD, summation of plastic displacements normalized by yield displacement) is plotted versus the SWDM fracture index recorded at a highly strained edge in the transition zone. As expected, the fracture demands in the transition zone are always larger under subassemblage as compared to uniaxial loading. However, it is important to note that the influence of rotational (i.e. subassemblage) loading on BRB fracture in the transitional zone highly depends on the configuration of BRBs. Therefore, the rotational loading effect can be mitigated by improving the detailed configuration of BRBs. Detailed FE analyses offer an important tool for BRB designers to improve the detailing of the transitional zone to be less susceptible to fracture.
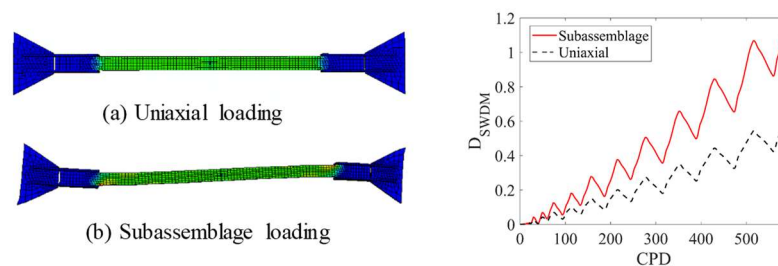

Fig. 9– Comparison of fracture damage index in transition zone

4. Fracture evaluation of BRBs and discussion

Using the FE simulation results and SWDM criterion, ductile fracture initiations observed in the experiments were evaluated. The Cumulative Density Functions (CDFs) of fracture at which fracture is likely to initiate (Fig.10) were computed following the probabilistic approach proposed by Myers et al.[17], that is:

$$F_{SWDM}(SWDM) = 1 - \left[1 - \hat{F}_{SWDM}(x_i, \hat{x_i})\right] \cdot P(\overline{E_1, E_2 \dots E_{i-1}}) \tag{7}$$

where $F_{SWDM}(SWDM)$ is unconditional probability that fracture has occurred before a particular point within any tensile portion of a loading history, $\hat{F}_{SWDM}(x_i, \hat{x_i})$ the complementary event of fracture (i.e. no fracture) before the x_i of the SWDM damage index value in the ith tensile cycle, $\hat{x_i}$ the initial SWDM damage index value in the ith tensile cycle.

Fig.10 shows the evaluation results of ductile fracture initiation for two representative experimental results. The WPSC3 specimen was tested under uniaxial loading and failed in the transitional zone, while the WPSC3A specimen was tested under subassemblage loading and failed in the yielding zone. Typically, BRBs are more likely to fracture in the transitional zone under subassemblage loading and in the yielding zone under uniaxial loading. However, different trends in the fracture locations are observed in the specimens shown in Fig.10, due to the observation that necking in the BRB core region tends to be greatly influenced by loading amplitude, whereas the amount of the damage accumulation in the transitional zone depends on a wider variety of factors (e.g. loading conditions, loading amplitudes and detailed configurations). Thus, the locations where fracture initiates may differ for each specimen depending on the specific circumstances in each test. Since the proposed FE simulation techniques can represent these effects, the proposed evaluation method successfully predicted the locations of fracture in the steel core.

For the WPSC3A specimen, the FE simulation captured well both where and when necking and ductile fracture initiation occurred. On the other hand, the fracture probabilities at which the WPSC3 specimen failed in the experiment greatly exceeded the median value of the ductile fracture criterion (i.e. the CPD at the median fracture probability of 0.5). This apparent discrepancy between the calculated CDF and point of observed failure may be attributed to the fact that the complete failure of the steel core is caused by the fracture mechanism described in Fig.2. This fracture process may occur suddenly when the local stress/strain field is sufficiently strong to cause rapid ductile crack propagation through the complete section (e.g. fracture in the yielding zone due to necking). On the other hand, failure tends to occur more gradually when the local stress/strain fields at the tip of an initiated ductile crack is not sufficiently high to propagate (e.g. fracture in the transitional zone under uniaxial loading and/or small amplitude loading). Therefore, for WPSC3 specimen, ductile fracture in the transitional zone may have initiated well before the complete failure of the steel core. Unser such conditions, since the proposed methodology evaluates ductile fracture initiation, the fracture evaluation results may be overly conservative. This observation highlights the necessity of research to develop computational and theoretical methodologies to accurately simulate the ductile crack propagation and subsequent cleavage fracture.
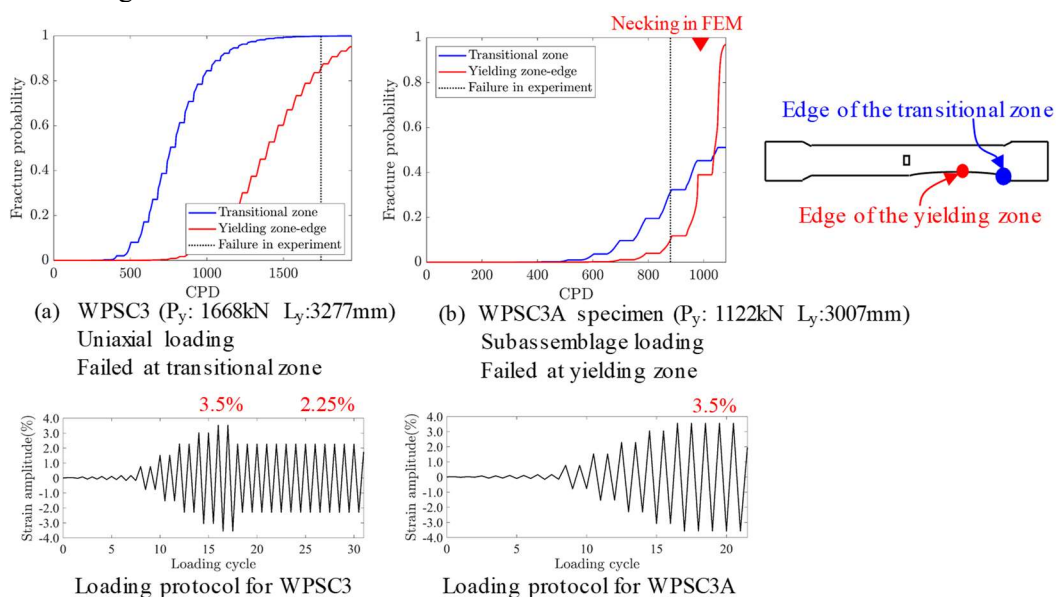

(a) WPSC3 (P_y: 1668kN L_y:3277mm)
Uniaxial loading
Failed at transitional zone

(b) WPSC3A specimen (P_y: 1122kN L_y:3007mm)
Subassemblage loading
Failed at yielding zone

Loading protocol for WPSC3

Loading protocol for WPSC3A

Fig. 10 – Simulated probabilities of ductile fracture initiation for BRB tests (a) WPSC3 and (b) WPSC3A

9

5. Seismic Collapse Safety of BRBFs Including BRB Fracture

5.1 Overview of the framework

In the next phase of this study, we integrated the detailed BRB FE fracture analyses with the overall response of BRBF systems with the overall goal to incorporate the likelihood of BRB fracture into BRBF collapse risk analyses. This study employed the concept of a reliability-based framework, so-called Hazard-Consistent Incremental Dynamic Analysis (HC-IDA) [18]. In this framework, the collapse spectral intensities obtained from conventional IDA are adjusted using two Intensity Measures (IMs), which represent frequency content (i.e., response spectrum shape) and duration of ground motions, both of which differ depending on the source of ground motions at a site, to evaluate site-specific collapse probabilities. This study expanded the HC-IDA to be applicable to evaluate site-specific BRB strain demand and fracture probabilities using frame analyses (i.e. IDA) and BRB fracture evaluation method described above, as schematically illustrated in Fig. 11. Details of this framework are summarized by Terashima [8].
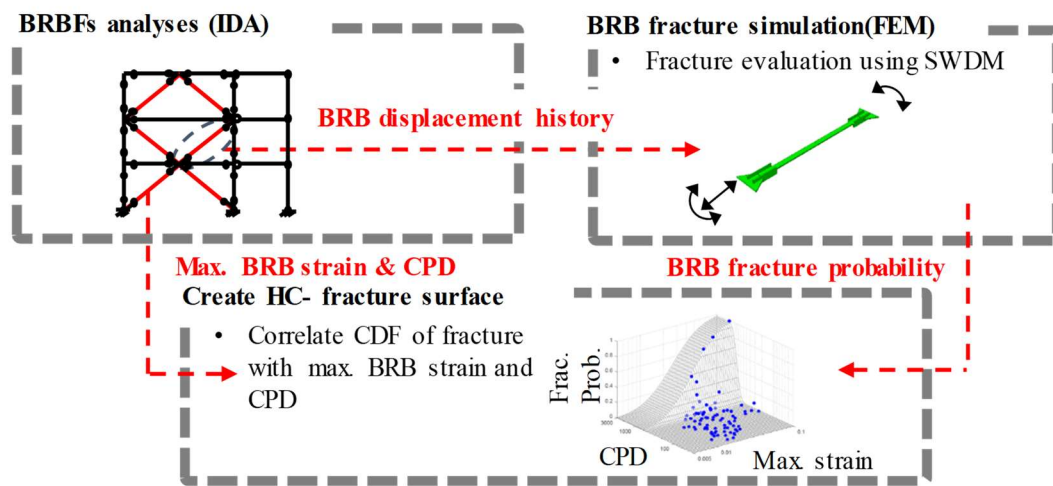

Fig. 11 – Framework for integrating detailed FE simulations with BRBF system assessment

5.2 Case study results

A total of 12 case studies were undertaken at two sites in the Western U.S. (i.e. a Los Angeles (LA) site and San Francisco (SF) site), studying two brace layouts (i.e. X-layout and single diagonal) for three different stories (3-, 6- and 12-story) at each site. As shown in Fig.12 (a), the BRB strain demands, particularly the cumulative strain demands, are larger for the SF site than those for the LA site. This difference is mainly caused by the expected magnitude of the ground motions for each site (mean magnitude at 2% in 50 years spectral intensity is $M_W7.6$ for the SF site and $M_W7.1$ for the LA site). Since larger magnitude earthquakes tend to cause longer duration ground motions, BRBs in the SF site tend to be subjected to larger cumulative strain demand, as compared with those in the LA site. In addition, the cumulative strain demand at the SF site exceeds the code-minimum demand capacity as specified in AISC341-16 [11], while the strain demand at the LA site is within the code requirements. Note that the code-minimum demand capacity was developed based on a few prior studies [19][20], both of which implicitly targeted for the sites nearby LA and did not consider the influences of site seismicity on BRB strain demands. This result implies that the current code specified strain demand capacity may not be sufficient for the BRB strain demands in some areas in the western U.S.

Fig.12 (b) shows the collapse fragility of BRBF systems, including BRB fracture as one of the non-simulated collapse modes of the BRBFs. The collapse fragility was shifted upward due to BRB fracture, showing that BRB fracture may greatly influence the collapse probabilities of BRBFs.
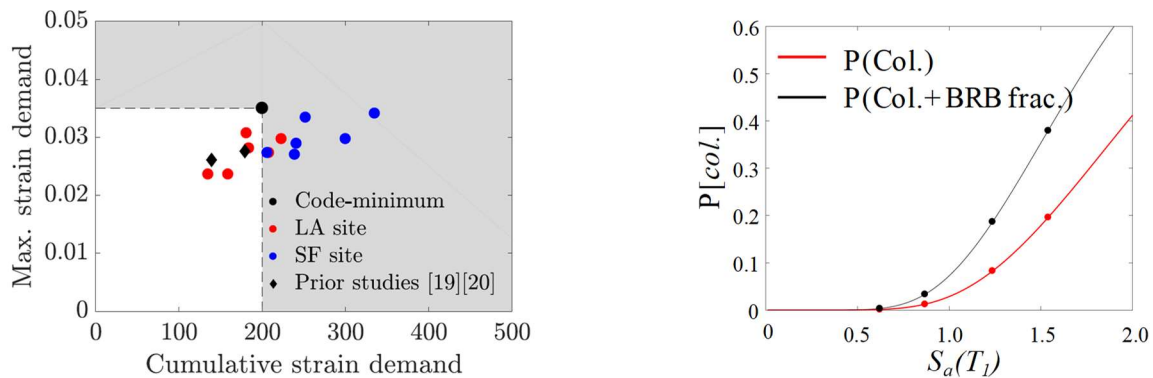
Fig. 12 – Results of BRBF systems analyses to quantify (a) median BRB plastic strain demands at MCE_R spectral intensities, and (b) including of BRB fracture on collapse of 6-story X-layout BRBF for SF Site

6. Concluding Remarks

This study has proposed a methodology to evaluate ductile fracture initiation of BRB steel core using detailed FE simulations with the Stress-Weighted Damage Model (SWDM) criterion for ductile fracture initiation. It incorporated several unique features of BRBs into the assessment of fracture initiation in the steel core. Since the proposed method can evaluate BRB fracture (i.e. ductility capacity) for various shapes and loading histories, it can be an effective tool for developing and verifying new BRB design applications, such as (a) for extremely large BRBs (e.g. outrigger systems) and (b) for BRBs subjected to higher strain demand than conventional BRBs. (e.g. energy dissipation devices for rocking frames). The proposed methodology evaluated the fracture in the yielding zone well, while it tended to overestimate the fracture in the transitional zone. These results may be attributed to the ductile fracture process mentioned above. When specimens failed in the yielding zone, the ductile fracture process occurs nearly instantaneously, while in the transitional zone, the fracture process gradually occurs as loading progresses. Since the proposed methodology evaluates ductile fracture initiation, it tends to overestimate complete failure of BRB specimens in the transitional zone. Research is currently being undertaken to develop a computational and theoretical methodology to evaluate ductile crack propagation and ductile-to-brittle conversion (i.e. cleavage fracture).

The study has also developed a framework to combine the detailed FE simulations of BRB fracture with nonlinear dynamic analyses to evaluate collapse risk in BRBF systems. This framework explicitly accounted for site seismicity using the two IMs (i.e. frequency contents and duration of ground motions). The results of the case studies with two different sites (i.e. SF and LA sites) indicate that BRB strain demands may differ depending on site seismicity, and current code-minimum strain demands may be unconservative for certain areas in the western U.S. These findings motivate us to better characterize BRB strain demands across varying building geometries and site seismicity. The proposed framework will assist in characterizing the brace ductility demands.

7. Acknowledgements

8. References

[1]   Kanvinde, A. and Deierlein, G.G. (2007) Cyclic Void Growth Model to Assess Ductile Fracture Initiation in Structural Steels due to Ultra Low Cycle Fatigue. *Journal of Engineering Mechanics*. 133 (6), 701–712.

11

[2] Nakamura, H., Takeuchi, T., Maeda, Y., Nakata, Y., Sasaki, T., Iwata, M., et al. (1999) Fatigue Properties of Practical-Scale Unbinded Braces. *Nippon Steel Corporation Technical Report*. 49–55.

[3] Takeuchi, T., Hajjar, J.F., Matsui, R., Nishimoto, K., and Aiken, I.D. (2012) Effect of local buckling core plate restraint in buckling restrained braces. *Engineering Structures*. 44 304–311.

[4] Anderson, T.L. (1995) Fracture Mechanics: Fundamentals and Application. 3rd ed. Taylor & Francis, .

[5] Kanvinde, A. and Deierlein, G.G. (2004) Micromechanical Simulation of Earthquake-Induced Fracture in Steel Structures. .

[6] Smith, C.M., Kanvinde, A.M., and Deierlein, G.G. (2014) A Stress-Weighted Damage Model for ductile fracture initiation in structural steel under cyclic loading and generalized stress states. .

[7] ABAQUS (2017) Abaqus CAE User's Manual version 2017. Dassault Systemes Simulia Corp, .

[8] Terashima, M. (2018) Ductile Fracture Simulation and Risk Quantification of Buckling-Restrained Braces Under Earthquakes, Stanford University, 2018.

[9] Budaházy, V. (2013) Modelling of the Hysteretic Behaviour of Buckling Restrained Braces. *Conference of Junior Researchers in Civil Engineering*. 34–41.

[10] Yoshida, K. and Kuriyama, Y. (2010) Numerical Analysis of Elasto-Plastic Behavior of Buckling Restrained Braces by Contact Analysis. *J. Struct. Constr. Eng., AIJ*. 75 (655), 1737–1743.

[11] AISC (2016) Seismic Provisions for Structural Steel Buildings (ANSI/AISC341-16). *American Society of Civil Engineering*.

[12] Saxey, B. and Daniels, M. (2014) Characterization of Overstrength Factors for Buckling Restrained Braces. in: Proc. Australas. Struct. Eng. Conf., Auckland, New Zealand.

[13] Pavlina, E.J. and Van Tyne, C.J. (2008) Correlation of Yield strength and Tensile strength with hardness for steels. *Journal of Materials Engineering and Performance*. 17 (6), 888–893.

[14] AISC (2010) Seismic Provisions for Structural Steel Buildings (ANSI/AISC341-10). *American Institute of Steel Construction*.

[15] Nishimoto, K., Nakata, Y., Aiken, I., Yamada, S., and Akira Wada (2004) Sub-Assembly Testing of Large Buckling-Restrained Unbonded Braces. in: 13th World Conf. Earthq. Eng., Vancouver.

[16] Tsai, K. and Hsiao, P. (2008) Pseudo-dynamic test of a full scale CFT/BRB frame-Part2; Seismic performance of buckling-restrained braces and connections. in: Pacific Conf. Earthq. Eng., pp. 1–6.

[17] Myers, A.T., Kanvinde, A.M., Deierlein, G.G., and Baker, J.W. (2014) Probabilistic Formulation of the Cyclic Void Growth Model to Predict Ultralow Cycle Fatigue in Structural Steel. *Journal of Engineering Mechanics*. 140 (6), 04014028.

[18] Chandramohan, R. (2016) Duration of Earthquake Ground Motion: Influence on Structural Collapse Risk and Integration on Design and Assessment Practice, Stanford University, 2016.

[19] Sabelli, R., Mahin, S., and Chang, C. (2003) Seismic demands on steel braced frame buildings with buckling-restrained braces. *Engineering Structures*. 25 (5), 655–666.

[20] Fahnestock, L. a., Sause, R., and Ricles, J.M. (2007) Seismic Response and Performance of Buckling-Restrained Braced Frames. *Journal of Structural Engineering*. 133 (9), 1195–1204.